Electrode Materials

International Edition: DOI: 10.1002/anie.201605096
German Edition: DOI: 10.1002/ange.201605096

Topotactic Consolidation of Monocrystalline CoZn Hydroxides for Advanced Oxygen Evolution Electrodes

*Jing Wang, Chuan Fu Tan, Ting Zhu, and Ghim Wei Ho**

Abstract: *We present a room temperature topotactic consolidation of cobalt and zinc constituents into monocrystalline CoZn hydroxide nanosheets, by a localized corrosion of zinc foils with cobalt precursors. By virtue of similar lattice orientation and structure coordination, the hybrid hydroxides amalgamate atomically without phase separation. Importantly, this in situ growth strategy, in combination with configurable percolated nanosheets, renders a high areal density of catalytic sites, immobilized structures, and conductive pathways between the nanosheets and underlying foils—all of which allow monocrystalline CoZn hydroxide nanosheet materials to function as effective electrodes for electrochemical oxygen evolution reactions. This convenient and eco-friendly topotactical transformation approach facilitates high-quality single crystal growth with improved multiphase purity and homogeneity, which can be extended to other transition metals for the fabrication of advanced functional nanocomposites.*

Topotactic transformation defines structural alteration within the crystal lattice (such as displacement or exchange of atoms) of a material, where the formed lattices inherit one or more crystallographic orientations from the initial precursor.[1] The prowess of topotactical conversion is that it supersedes equilibrium crystal shapes/habits, thereby allowing phase to be correlated with coordinated structures at atomic homogeneity.[2] Nonetheless, obtaining high-quality monocrystalline topochemical reactions is still a challenge and often demands high-temperature processes[3] or expensive equipment, such as ultrahigh vacuum pulsed laser,[4] thereby making the technique impractical for large-scale applications. Furthermore, reported topotactic transformations, such as metal oxidization,[5] phase transition,[6] and conversion of hydroxides into oxides or metals,[7] primarily involve a single metal cation, which precludes formation of bi-/multinary constituents. In the context of the ability of multi-component materials to alter electronic states that exhibit strong interplay between the strength of surface intermediate bonds and electrochemical reactivity,[8] it is essential to readily access topotactic consolidation of two or more constituents within a homogeneous entity.

Herein, we demonstrate a mild room temperature topotactic consolidation of cobalt–zinc hydroxides (CZH) with an ensemble of nanosheets, by an in situ corrosion of zinc foils mediated by cobalt precursors. The defining advantage of such a metal corrosion technique is its undeniably simple low-cost route, which enables spontaneous electrochemical dissolution–redeposition without the expense of external energy. The chemical etching dissolves metals into their ion derivatives, which further self-assemble into their respective oxides or inorganic salts.[9] Though less appreciated, the conversion of metallic substrates into their constituent materials involves a topotactic reconstruction of crystal lattices, as per the crystal habit of the employed precursor. By virtue of similar lattice orientation and coordinated structure, hybrid cobalt–zinc ionic species amalgamate with atomic homogeneity to produce monocrystalline hydroxides, circumventing the phase separation issue. The configurable percolated CZH nanosheets interface directly with zinc foils, and present mechanically stable structures for superior electrical conductivity, increased areal density of active sites, and superaerophobic surfaces that benefit diffusion of electrolyte and gas bubbles. Hence, the characteristics of efficient electrodes for electrochemical oxygen evolution reactions (OER) are established.

Corrosion with a small amount of $CoCl_2$ solution induces a topotactic conversion of the zinc foil surface into well-defined hydroxide nanosheet structures. The localized corrosion areas are homogeneously covered by densely packed and vertically oriented nanosheets (Figure 1), in which varying cobalt concentrations lead to dissimilar structures. A low concentration of 0.01 M (CZH-1) yields individual clusters (ca. 5 μm width) of thin hexagonal nanosheets, while a higher 0.05 M concentration forms an interconnected network of nanosheets (CZH-2). The nanosheets are approximately 300 nm thick with a uniform dispersion, and are quasi continuous in the case of 0.1 M (CZH-3). A further increase in concentration to 0.5 M results in thicker nanosheets up to about 900 nm (CZH-4). This in situ formation of immobilized nanosheets constitutes firm adhesion to the underlying zinc substrates.

Crystal structures and the chemical constitution of the nanosheets were analyzed. A representative TEM image of CZH-3 in Figure 2a shows an individual nanosheet and its SAED pattern demonstrates an apparent monocrystalline character with hexagonal symmetry (Figure 2b), in which the

[*] Dr. J. Wang, C. F. Tan, Dr. T. Zhu, Prof. Dr. G. W. Ho
Department of Electrical and Computer Engineering
National University of Singapore
4 Engineering Drive 3, Singapore 117583 (Singapore)
E-mail: elehgw@nus.edu.sg
Prof. Dr. G. W. Ho
Engineering Science Programme, National University of Singapore
9 Engineering Drive 1, Singapore 117575 (Singapore)
and
Institute of Materials Research and Engineering, A*STAR (Agency for Science, Technology and Research)
2 Fusionopolis Way, Singapore 138634 (Singapore)
Supporting information and the ORCID identification number(s) for the author(s) of this article can be found under http://dx.doi.org/10.1002/anie.201605096.

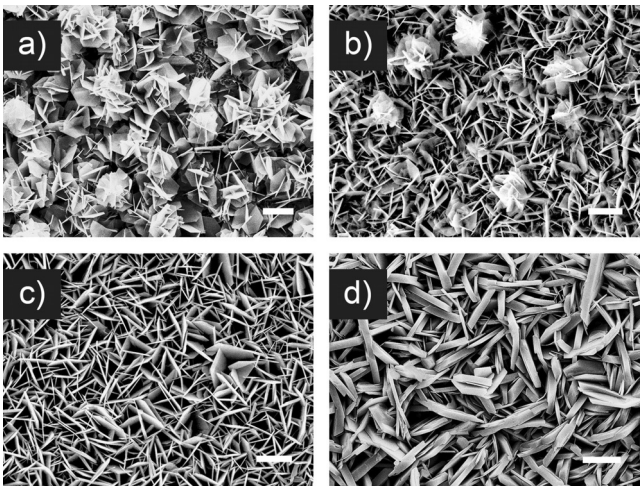

Figure 1. SEM images of CZH nanosheets obtained from cobalt concentrations of a) 0.01 M, b) 0.05 M, c) 0.1 M, and d) 0.5 M. Scale bar: 5 μm.

indexed (110), (010), and (100) crystal planes correspond to hydroxide forms of cobalt and zinc.[10] In the HRTEM image (Figure 2c), a well-resolved periodic crystal lattice without distortion is observed, with an interfringe angle of 60° and spacing distances of 2.37 and 2.52 Å. The monocrystalline attribute without grain boundaries is believed to favor electrical conductivity of the nanosheets. Elemental mapping images (area of the sheet edge) and EDX analysis present an even dispersion of cobalt, zinc, oxygen, and chloride elements (Figure 2d,e). Significantly, the XRD spectra (Figure 2f) exhibit diffraction peaks that can be indexed to α-$Co(OH)_2$ (JCPDS card: 02-0925) and $Zn_5(OH)_8Cl_2{\cdot}H_2O$ (JCPDS card: 07-0155), revealing a successful hybridization of cobalt and zinc hydroxides. Accordingly, the fringe spacings of 2.37 and 2.52 Å are assigned to (110) and (100) planes of both α-$Co(OH)_2$ and $Zn_5(OH)_8Cl_2{\cdot}H_2O$. The prominent diffraction peak located at $2\theta = 11.6°$ for both hydroxides, shows their preferential growth along the [003] direction. Noticeably, hydrotalcite-like α-$Co(OH)_2$ and simonkolleite-like $Zn_5(OH)_8Cl_2{\cdot}H_2O$ have a rhombohedral coordination geometry. Furthermore, $Co(OH)_2$ tends to grow into sheets or platelets because of its intrinsic lamellar structures, and $Zn_5(OH)_8Cl_2{\cdot}H_2O$ usually presents a sheet-like architecture.[10b] The similar lattice orientation and structure coordination of the two hydroxides contributes to phase amalgamation, resulting in thermodynamically stable CoZn hydroxides. Chemical compositions of these nanosheets are further understood by considering their functional groups and electronic states. In the FTIR spectra (Figure 2g), the absorption bands at 3450 cm^{-1} are ascribed to O-H stretching vibrations of hydrogen-bonded hydroxyl groups and interlayer water molecules, while 1605 cm^{-1} is assigned to the bending modes of water molecules. The stretching vibrations at 1045 cm^{-1} probably arise from intercalated anions (Cl^-).[11] The absorption peaks below 1000 cm^{-1} are likely associated with Co-O/Zn-O stretching and Co-OH/Zn-OH bending vibrations.[11,12] In the XPS spectra (Figure 2h–j), binding energies fitted to 781.1, 783.2, and 797.3 eV in the Co 2p region are attributed to divalent Co^{2+}. The absence of trivalent Co^{3+} (778.9 eV) suggests that α-$Co(OH)_2$ is stable without oxidation under ambient conditions. The peaks located at 1022.0 and 1045.1 eV are ascribed to Zn $2p_{3/2}$ and Zn $2p_{1/2}$, respectively. In the O 1s region, binding energies at 531.4 and 532.2 eV are identified as Co-O/Zn-O and OH groups, respectively. Also distinguishable are Cl 2p peaks at 198.6 and 200.0 eV (Supporting Information, Figure S1). Collectively, the as-formed nanosheets demonstrate a high structural and chemical integrity of monocrystalline CoZn hydroxides.

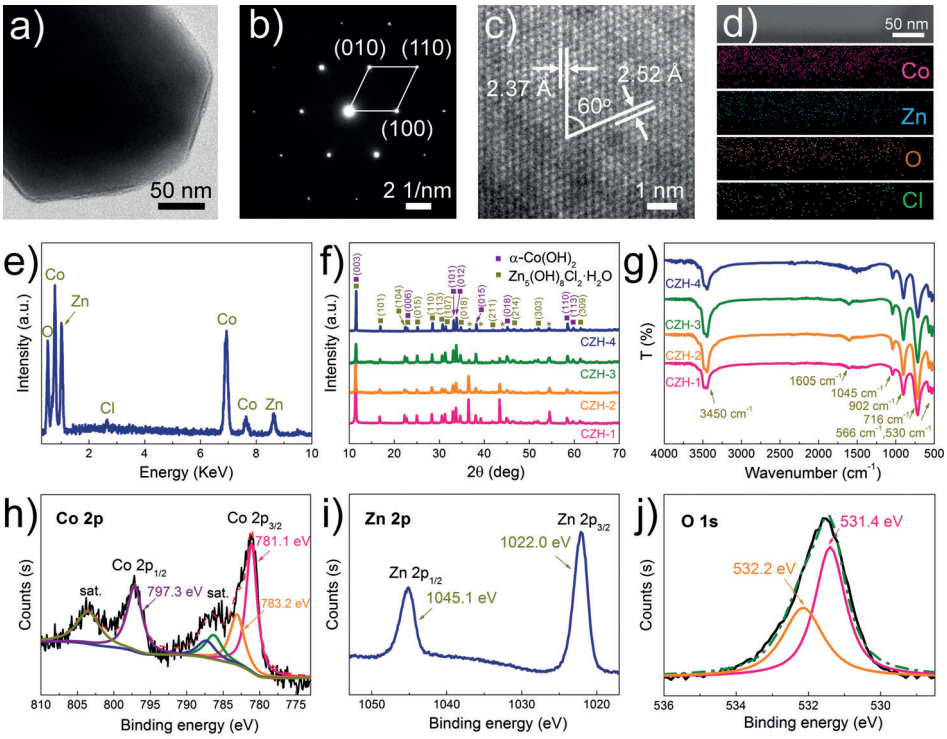

Figure 2. a) TEM image, b) SAED pattern, c) HRTEM image, d) elemental mappings, and e) EDX spectrum of CZH-3. f) XRD spectra (an asterisk indicates zinc foil), and g) FTIR spectra of CoZn hydroxides. h) Co 2p, i) Zn 2p, and j) O 1s high-resolution XPS spectra of CZH-3.

To explore the formation mechanism of CZH nanosheets, time-dependent morphology evolution of CZH-3 was recorded. Before corrosion starts, bare zinc foil presents

a pristine surface (Supporting Information, Figure S2). Dispensing cobalt solutions onto the surface of zinc foils leads to an immediate release of gas bubbles. The SEM image taken at this stage (Figure 3a) shows sparsely distributed

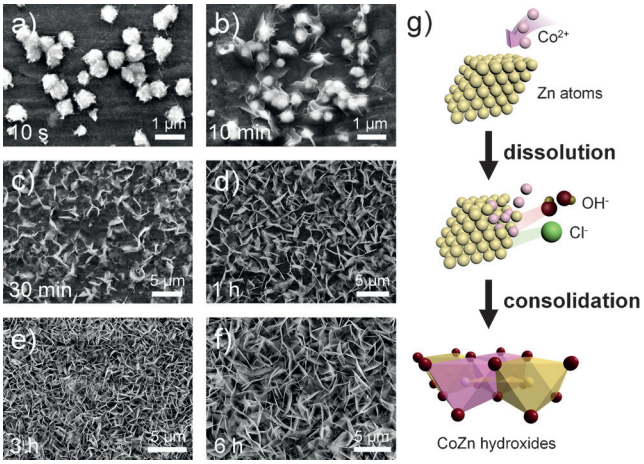

Figure 3. Morphology evolution of CZH-3 at corrosion durations of a) 10 s, b) 10 min, c) 30 min, d) 1 h, e) 3 h, and f) 6 h. g) Mechanism of CoZn hydroxide formation.

hierarchical nanoparticles (NPs) coated with smaller particles, consisting of cobalt, zinc, oxygen, and chloride elements (Supporting Information, Figure S3). Shortly after 10 min, a hybrid structure of NPs enveloped within ultrathin sheets is observed (Figure 3b), with their chemical constituents remaining unchanged (Supporting Information, Figure S4). The partial structural deformation, along with the particle size decreasing from about 700 to less than 500 nm, implies that cobalt corrosion readily shapes NPs into sheet-like structures. When corrosion is prolonged to 30 min, only irregular thin sheets are observed on the foil surfaces. These sheets further grow and agglomerate as corrosion continues, ultimately giving rise to an ensemble of interconnected uniform nanosheets (Figure 3d–f and Figure 1c). The XRD spectrum recorded at the three hour mark shows a small diffraction peak at 11.6°, indicating that hydroxides will grow along the [003] direction (Supporting Information, Figure S5). Moreover, the atom ratios of cobalt increase while that of zinc decreases with corrosion (Supporting Information, Figure S6), suggesting that cobalt is progressively incorporated with zinc. On the basis of the morphology evolution, the mechanism of nanosheet formation is proposed in Figure 3g. Metal corrosion involves two half electrochemical reactions, namely an anodic reaction (metals lose electrons) and a cathodic reaction (non-metals consume electrons).[9a] Initially, cobalt solutions with pH values ranging from 5.61 to 6.27 (Supporting Information, Figure S7) provide a mild acidic environment for Zn^0 to be oxidized into Zn^{2+} ions at the anode (see Equation (1)).

$$Zn_{(s)} \rightarrow Zn^{2+}{}_{(aq)} + 2\,e^- \quad (1)$$

As a result of the change of free energy originating from their differences in reduction potential,[13] the dissipated Co^{2+} ions will attack the defects to occupy the vacancies after zinc dissolution, thus inducing a localized topochemical conversion into a CoZn composite. Meanwhile, the generated electrons migrate to the cathode and couple with oxygen from air to form OH^- groups (see Equation (2)).[9e,14]

$$^1/_2\,O_{2(g)} + H_2O_{(l)} + 2\,e^- \rightarrow 2\,OH^-{}_{(aq)} \quad (2)$$

Surrounded by anion domains, metal ions coordinate with OH^- groups (Zn^{2+} easily adsorbs Cl^-) and subsequently self-assemble into CoZn intermediate NPs (see Equations (3) and (4)).

$$5\,Zn^{2+}{}_{(aq)} + 8\,OH^-{}_{(aq)} + 2\,Cl^-{}_{(aq)} + H_2O_{(l)} \rightarrow Zn_5(OH)_8Cl_2 \cdot H_2O_{(s)} \quad (3)$$

$$Co^{2+}{}_{(aq)} + 2\,OH^-{}_{(aq)} \rightarrow Co(OH)_{2(s)} \quad (4)$$

The topotactic consolidation continues when more Co^{2+} ions are inserted, ultimately sculpturing the NPs into sheet-like ensembles with a monocrystalline lattice. Indeed, $Zn_5(OH)_8Cl_2{\cdot}H_2O$ is easily attainable from atmospheric corrosion of zinc-containing metals at pH values of 5.5 to 8.5 in a chloride environment, such as sodium chloride (Supporting Information, Figure S8).[15] The diversity of the nanosheets correlates with the corrosion kinetics determined by pH values and etchant concentrations. Concentrated $CoCl_2$ solutions afford higher acidity, which induces a faster dissolution of zinc atoms from foils, resulting in release of a higher concentration of zinc ions. As a result, the nanosheets become larger and thicker at higher cobalt concentrations, and 0.1 M is optimal to form uniformly interlocked nanosheets. This simple topotactic conversion is extendable to other metal substrates and etchants to achieve the desired nanostructures (Supporting Information, Figures S9 and S10).

Given their high electrochemical activity and interlayer chemistry,[16] cobalt hydroxides have been extensively explored as electrocatalysts to lower the overpotential barrier for OER in electrocatalytic water splitting.[17] In this case, CZH-coated zinc foils are used as direct electrodes (without post-treatments) for electrochemical OER in alkaline media. Their polarization curves are achieved from LSV measurements in 0.1 M and 1 M KOH electrolytes (scan rate: 5 $mV\,s^{-1}$), in which current densities are normalized by the geometric area of electrodes. During the electrochemical process, large quantities of gas bubbles are generated and collected from both platinum and CZH electrodes; hydrogen and oxygen, respectively, were identified by gas chromatography (data not shown). In Figure 4a, the electrodes present onset potentials of approximately 1.7 V (vs. RHE), beyond which current densities rise rapidly with the increase of applied potentials. CZH-3 exceeds other electrodes in current density across all potentials, showing the highest electrochemical activity for oxygen evolution. To deliver a current density of 10 $mA\,cm^{-2}$, the overpotentials of CZH electrodes are calculated to be 0.63 V (CZH-3, green line). Similar trends are observed in the case of 1 M KOH, with much higher current densities than that observed for 0.1 M KOH. Importantly, the onset potential of the best-performing CZH-3 reached 1.58 V in 1 M KOH with

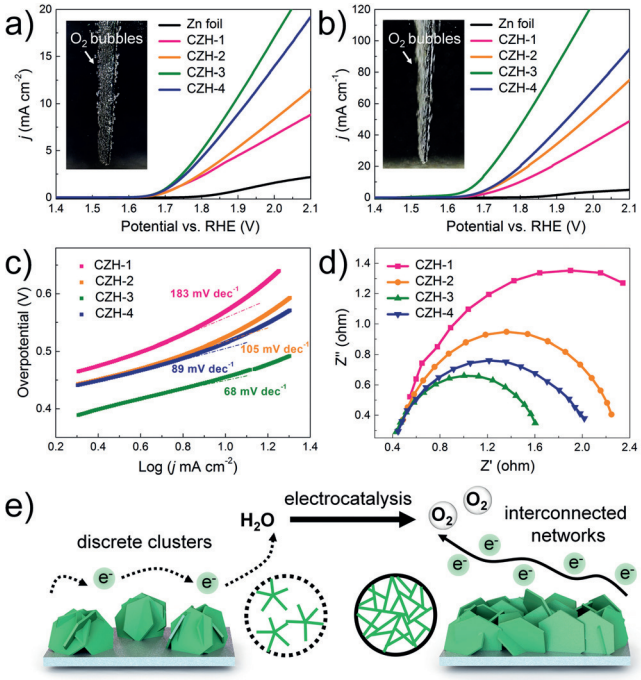

Figure 4. LSV curves of CZH nanosheets performed in a) 0.1 M and b) 1 M KOH electrolytes. Inset images: digital photos of the CZH-3 electrode during the OER process. c) Tafel plots and d) EIS spectra of CZH nanosheets recorded in KOH (1 M) electrolyte. e) Two models (top- and cross-sectional views) illustrating the conductive networks of the nanosheets.

a low overpotential of 0.43 V, which is comparable to recently reported cobalt-based electrocatalysts (Supporting Information, Tables S1). This is also validated by a much faster generation of oxygen bubbles (Figure 4a,b inset). It is noted that pure $Zn_5(OH)_8Cl_2{\cdot}H_2O$ and pure α-$Co(OH)_2$ are incapable of achieving high current density individually (Supporting Information, Figures S11 and S12), hence the synergistic effect of the two hydroxides is responsible for the enhanced OER kinetics. Comparatively, bare zinc foils exhibit an inferior OER response, failing to reach a current density of 10 mA cm^{-2} even at a high potential of 2.1 V in either 0.1 M or 1 M KOH solutions (black line). Moreover, zinc foils suffer from electrochemical deterioration after measurements (Supporting Information, Figure S13), while CZH electrodes are stable and retain their morphologies well (Supporting Information, Figure S14). This demonstrates that CZH nanosheets can also function as a protective layer to prevent the destruction of zinc foils. The fitted Tafel plots of CZH electrodes based on log (j) ~ η show slopes of 183, 105, 68, and 89 mV dec^{-1} for CZH-1, CZH-2, CZH-3, and CZH-4, respectively (Figure 4c), indicating that the improved OER reaction kinetics result from enhanced electron transfer.[18] In essence, high conductivity is critical to evaluate the performance of an electrocatalyst.[19] Therefore, EIS spectra of CZH electrodes in 1 M KOH solution were obtained (Figure 4d). The Nyquist plots reveal that charge transfer resistance controls the kinetics at the electrode interfaces. CZH-3 shows the smallest charge transfer resistance among all the electrodes, exhibiting superior electron mobility. Typically, CZH-3 demonstrates good durability of current densities for 10 h (Supporting Information, Figure S15).

Fundamentally, OER involves three stages; namely, 1) the adsorption of water molecules onto electrode surfaces, 2) electron transfer between the two electrodes, and 3) splitting of water into hydrogen and oxygen on the respective electrodes. The hydrophilic hydroxyl groups in CZH are beneficial for adsorption of water molecules at the electrode surfaces. The nanosheet structures are believed to exhibit superaerophobicity for a quick removal of small bubbles at electrode–electrolyte interfaces.[20] Moreover, highly exposed active sites with monocrystalline character contribute to favorable electron transfer, thus facilitating the OER process. The difference in OER performances of the nanosheets is possibly related to their distinctive structures (Figure 4e; Supporting Information, Figure S16) and chemical compositions (Supporting Information, Table S2). CZH-1 presents discontinuous conductive networks, in which adjacent discrete spatial clustering of nanosheets is observed. Conversely, the continuously interlocked nanosheets (CZH-3) construct extended conductive networks, forming efficient electron transport pathways to accelerate OER kinetics.[21] Moreover, CZH-3 has a higher cobalt ratio than that of CZH-1 and CZH-2, suggesting an increased number of active sites provided by α-$Co(OH)_2$ that are able to benefit electrocatalytic OER. The thicker nanosheets in CZH-4 reduce the specific surface area of catalytic sites (despite the fact that it possesses the highest cobalt ratios and interconnected networks) leading to decreased OER performance in contrast to CZH-3.

In summary, we have described a successful topotactic consolidation of monocrystalline CoZn hydroxide nanosheets by an in situ corrosion of zinc foils with cobalt chloride. The similar lattice orientation and structure coordination features of the nanosheets contribute to phase amalgamation of the two constituents with thermodynamic stability. The percolated nanosheets are endowed with hydrophilic functional groups, superaerophobic surfaces, and highly exposed active sites, which directly serve as electrodes for electrochemical oxygen evolution reactions. By virtue of quasi continuous interlocked conjunctions for efficient electron transport, the nanosheets show a low overpotential of 0.43 V and a Tafel slope of 68 mV dec^{-1}. This simple approach is feasible for fabrication of functional nanocomposites with improved multiphase purity and homogeneity for electrical, catalytic, and photochemical applications.

Acknowledgements

This work is supported by MOE R-263-000-B38-112 and R-263-000-B63-112 (Ministry of Education, Singapore).

Keywords: cobalt hydroxide · electrocatalysis · oxygen evolving reactions · single crystals · topotactic transitions

How to cite: *Angew. Chem. Int. Ed.* **2016**, *55*, 10326–10330
Angew. Chem. **2016**, *128*, 10482–10486

[1] R. D. Shannon, R. C. Rossi, *Nature* **1964**, *202*, 1000 – 1001.
[2] K. D. Demadis, M. Papadaki, M. A. G. Aranda, A. Cabeza, P. Olivera-Pastor, Y. Sanakis, *Cryst. Growth Des.* **2010**, *10*, 357 – 364.
[3] a) J.-Y. Kim, D. Lee, H. J. Kim, I. Lim, W. I. Lee, D.-J. Jang, *J. Mater. Chem. A* **2013**, *1*, 5982 – 5988; b) C. F. Guo, S. Cao, J. Zhang, H. Tang, S. Guo, Y. Tian, Q. Liu, *J. Am. Chem. Soc.* **2011**, *133*, 8211 – 8215.
[4] T. Mairoser, J. A. Mundy, A. Melville, D. Hodash, P. Cueva, R. Held, A. Glavic, J. Schubert, D. A. Muller, D. G. Schlom, A. Schmehl, *Nat. Commun.* **2015**, *6*, 7716.
[5] J. Yang, Q. Wu, S. He, J. Yan, J. Shi, J. Chen, M. Wu, X. Yang, *Nanoscale* **2015**, *7*, 13888 – 13897.
[6] C. Wei, Q. Lu, J. Sun, F. Gao, *Nanoscale* **2013**, *5*, 12224 – 12230.
[7] a) R. Ma, M. Osada, L. Hu, T. Sasaki, *Chem. Mater.* **2010**, *22*, 6341 – 6346; b) Y. Kuang, G. Feng, P. Li, Y. Bi, Y. Li, X. Sun, *Angew. Chem. Int. Ed.* **2016**, *55*, 693 – 697; *Angew. Chem.* **2016**, *128*, 703 – 707.
[8] a) S. Pan, L. He, J. Peng, F. Qiu, Z. Lin, *Angew. Chem. Int. Ed.* **2016**, DOI: 10.1002/anie.201603189; *Angew. Chem.* **2016**, DOI: 10.1002/ange.201603189; b) X. Pang, C. Wan, M. Wang, Z. Lin, *Angew. Chem. Int. Ed.* **2014**, *53*, 5524 – 5538; *Angew. Chem.* **2014**, *126*, 5630 – 5644; c) H. Xu, X. Pang, Y. He, M. He, J. Jung, H. Xia, Z. Lin, *Angew. Chem. Int. Ed.* **2015**, *54*, 4636 – 4640; *Angew. Chem.* **2015**, *127*, 4719 – 4723.
[9] a) H.-D. Yu, Z. Zhang, M.-Y. Han, *Small* **2012**, *8*, 2621 – 2635; b) J. Wang, G. W. Ho, *Angew. Chem. Int. Ed.* **2015**, *54*, 15804 – 15808; *Angew. Chem.* **2015**, *127*, 16030 – 16034; c) F. U. Renner, A. Stierle, H. Dosch, D. M. Kolb, T. L. Lee, J. Zegenhagen, *Nature* **2006**, *439*, 707 – 710; d) C. Lu, L. Qi, J. Yang, L. Tang, D. Zhang, J. Ma, *Chem. Commun.* **2006**, 3551 – 3553; e) S. Wang, L. Feng, L. Jiang, *Adv. Mater.* **2006**, *18*, 767 – 770.
[10] a) S. Bae, J.-H. Cha, J. H. Lee, D.-Y. Jung, *Dalton Trans.* **2015**, *44*, 16119 – 16126; b) H. Chen, L. Zhu, H. Liu, W. Li, *Electrochim. Acta* **2013**, *105*, 289 – 298.
[11] B. Hu, S.-F. Chen, S.-J. Liu, Q.-S. Wu, W.-T. Yao, S.-H. Yu, *Chem. Eur. J.* **2008**, *14*, 8928 – 8938.
[12] Z. Liu, R. Ma, M. Osada, K. Takada, T. Sasaki, *J. Am. Chem. Soc.* **2005**, *127*, 13869 – 13874.
[13] J. F. Betz, W. W. Yu, Y. Cheng, I. M. White, G. W. Rubloff, *Phys. Chem. Chem. Phys.* **2014**, *16*, 2224 – 2239.
[14] a) Z. Zhang, X. Shao, H. Yu, Y. Wang, M. Han, *Chem. Mater.* **2005**, *17*, 332 – 336; b) Y. Fang, Q. Pang, X. Wen, J. Wang, S. Yang, *Small* **2006**, *2*, 612 – 615; c) J. Liu, X. Huang, Y. Li, K. M. Sulieman, X. He, F. Sun, *J. Mater. Chem.* **2006**, *16*, 4427 – 4434.
[15] R. Lindström, J. E. Svensson, L. G. Johansson, *J. Electrochem. Soc.* **2000**, *147*, 1751 – 1757.
[16] L.-B. Kong, J.-W. Lang, M. Liu, Y.-C. Luo, L. Kang, *J. Power Sources* **2009**, *194*, 1194 – 1201.
[17] a) J. Wang, W. Cui, Q. Liu, Z. Xing, A. M. Asiri, X. Sun, *Adv. Mater.* **2016**, *28*, 215 – 230; b) H. Liang, F. Meng, M. Cabán-Acevedo, L. Li, A. Forticaux, L. Xiu, Z. Wang, S. Jin, *Nano Lett.* **2015**, *15*, 1421 – 1427; c) C. Qiao, Y. Zhang, Y. Zhu, C. Cao, X. Bao, J. Xu, *J. Mater. Chem. A* **2015**, *3*, 6878 – 6883; d) S. Chen, J. Duan, M. Jaroniec, S. Z. Qiao, *Angew. Chem. Int. Ed.* **2013**, *52*, 13567 – 13570; *Angew. Chem.* **2013**, *125*, 13812 – 13815; e) C. C. L. McCrory, S. Jung, J. C. Peters, T. F. Jaramillo, *J. Am. Chem. Soc.* **2013**, *135*, 16977 – 16987; f) J.-X. Feng, L.-X. Ding, S.-H. Ye, X.-J. He, H. Xu, Y.-X. Tong, G.-R. Li, *Adv. Mater.* **2015**, *27*, 7051 – 7057.
[18] a) L. Xu, Q. Jiang, Z. Xiao, X. Li, J. Huo, S. Wang, L. Dai, *Angew. Chem. Int. Ed.* **2016**, *55*, 5277 – 5281; *Angew. Chem.* **2016**, *128*, 5363 – 5367; b) P. Chen, K. Xu, T. Zhou, Y. Tong, J. Wu, H. Cheng, X. Lu, H. Ding, C. Wu, Y. Xie, *Angew. Chem. Int. Ed.* **2016**, *55*, 2488 – 2492; *Angew. Chem.* **2016**, *128*, 2534 – 2538; c) C. Xia, Q. Jiang, C. Zhao, M. N. Hedhili, H. N. Alshareef, *Adv. Mater.* **2016**, *28*, 77 – 85; d) Y. Jin, H. Wang, J. Li, X. Yue, Y. Han, P. K. Shen, Y. Cui, *Adv. Mater.* **2016**, *28*, 3785 – 3790.
[19] J.-X. Feng, H. Xu, Y.-T. Dong, S.-H. Ye, Y.-X. Tong, G.-R. Li, *Angew. Chem. Int. Ed.* **2016**, *55*, 3694 – 3698; *Angew. Chem.* **2016**, *128*, 3758 – 3762.
[20] a) Z. Lu, W. Zhu, X. Yu, H. Zhang, Y. Li, X. Sun, X. Wang, H. Wang, J. Wang, J. Luo, X. Lei, L. Jiang, *Adv. Mater.* **2014**, *26*, 2683 – 2687; b) Z. Lu, W. Xu, W. Zhu, Q. Yang, X. Lei, J. Liu, Y. Li, X. Sun, X. Duan, *Chem. Commun.* **2014**, *50*, 6479 – 6482; c) M. S. Faber, R. Dziedzic, M. A. Lukowski, N. S. Kaiser, Q. Ding, S. Jin, *J. Am. Chem. Soc.* **2014**, *136*, 10053 – 10061.
[21] Y. Zhang, B. Wu, Y. Tang, D. Qi, N. Wang, X. Wang, X. Ma, T. C. Sum, X. Chen, *Small* **2016**, *12*, 2291 – 2299.

Received: May 25, 2016
Revised: June 14, 2016
Published online: July 15, 2016

